

Numerical modelling of gas flow in a compact clay barrier for DECOVALEX-2019

Tamayo-Mas, E. and Harrington, J.F.

British Geological Survey, Keyworth, Nottingham, United Kingdom

Shao, H.

Federal Institute for Geosciences and Natural Resources, Hanover, Germany

Dagher, E.E.

Canadian Nuclear Safety Commission/University of Ottawa, Ottawa, Ontario, Canada

Lee, J.

Korea Atomic Energy Research Institute, Daejeon, Korea

Kim, K. and Rutqvist, J.

Lawrence Berkeley National Laboratory, Berkeley, California, U.S.A.

Lai, S.H.

Center for Advanced Model Research Development and Applications, National Central University, Taoyuan, Taiwan, R.O.C.

Chittenden, N.

Quintessa Ltd, Henley-on-Thames, Oxfordshire, United Kingdom

Wang, Y.

Sandia National Laboratories, Albuquerque, New Mexico, U.S.A.

Damians, I.P. and Olivella, S.

Universitat Politècnica de Catalunya, Barcelona, Spain

ABSTRACT: The mechanisms controlling the movement of gases through geological disposal facilities can be described by models accounting for (i) diffusion, (ii) two-phase flow, (iii) localised flow pathways and (iv) gas fracturing of the rock. It is therefore necessary to consider all these phenomena for a better understanding of the processes governing the movement of gases in low permeability materials. The purpose of Task A in the current phase of the DEvelopment of COupled models and their VALidation against Experiments (DECOVALEX) project is to better understand the processes governing the advective movement of gas. In this paper, a synthesis of the ongoing work of eight participating modelling teams is presented. A wide range of 2D and 3D approaches including (i) continuous strategies assuming different mechanical deformation behaviors, (ii) continuous models with distinct phases or embedded fractures and (iii) discrete models with different formulations are validated against a gas flow test on pre-compacted bentonite undertaken by the British Geological Survey. The results of the ongoing work show that after a calibration process, plausible descriptions of the laboratory experiment can be achieved.

1. INTRODUCTION

The processes governing the movement of repository gases through engineered barriers and argillaceous host rocks can be split into two components, (i) molecular diffusion (governed by Fick's Law) and (ii) bulk advection. In the case of a repository for radioactive waste, corrosion of metallic materials under anoxic conditions will lead to the formation of hydrogen. Radioactive decay of the waste and the radiolysis of water are additional source terms. If the rate of gas production exceeds the rate of gas diffusion within the pores of the barrier or host rock, a discrete gas phase will form

(Wikramaratna et al., 1993; Ortiz et al., 2002; Weetjens and Sillen, 2006). Under these conditions, gas will continue to accumulate until its pressure becomes sufficiently large for it to enter the surrounding material.

In clays and mudrocks, four primary phenomenological models describing gas flow can be defined, see Figure 1: (1) gas movement by diffusion and/or solution within interstitial fluids along prevailing hydraulic gradients; (2) gas flow in the original porosity of the fabric, commonly referred to as two-phase flow; (3) gas flow along localised dilatant pathways, which may or may not interact with the continuum stress field; and (4) gas fracturing of the rock

similar to that performed during hydrocarbon stimulation exercises.

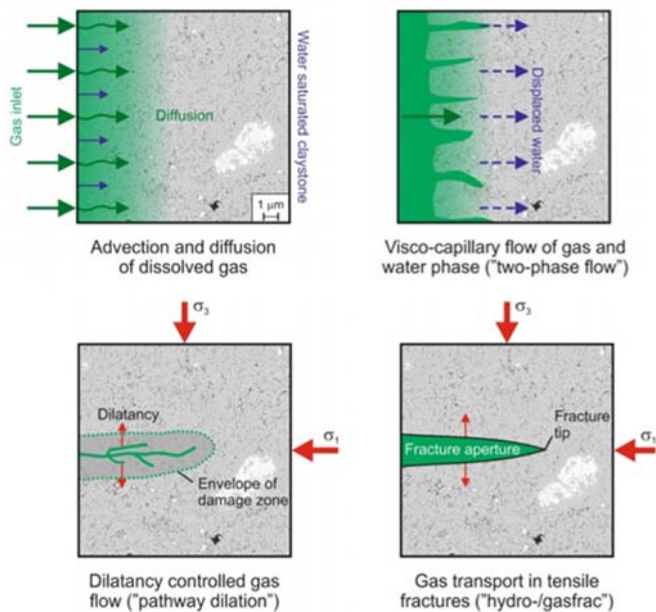


Fig. 1. Conceptual models of gas flow (after Marschall et al. 2005).

There is now a growing body of evidence (Horseman et al., 1996, 2004; Harrington and Horseman, 1999, 2003; Angeli et al., 2009; Harrington et al., 2017a and b) that in the case of plastic clays and in particular bentonite, classic concepts of porous medium two-phase flow are inappropriate and continuum approaches to modelling gas flow may be questionable, depending on the scale of the processes and resolution of the numerical model. However, the detail of the dilatant mechanisms controlling gas entry, flow and pathway sealing are unclear and the “memory” of such features within clay may impair barrier performance, in particular, acting as preferential flow paths for the movement of radionuclides.

As such, development of new and novel numerical representations for the quantitative treatment of advective gas flow in clay-based repository systems are therefore required, and are the primary focus of Task A in the current phase of the DECOVALEX (D-2019) project. The DECOVALEX project is an international research and model comparison collaboration aiming to enhance the understanding of coupled thermo-hydro-mechanical processes for geological disposal of radioactive waste, see <http://decovallex.org/> for more information.

New numerical techniques provide an invaluable tool with which to assess the impact of gas flow on repository layout and therefore design of any future facility. In addition, the same processes and mechanisms described in such models are of direct relevance to other clay-based engineering issues where immiscible gas flow is involved

e.g. shale gas, hydrocarbon migration, carbon capture and storage, and landfill design.

This paper provides a summary of the work conducted to date by the following participating modelling teams:

- (i) BGR/UFZ (Germany): Federal Institute for Geosciences and Natural Resources and the Helmholtz Centre for Environmental Research.
- (ii) CNSC (Canada): Canadian Nuclear Safety Commission.
- (iii) KAERI (Korea): Korea Atomic Energy Research Institute.
- (iv) LBNL (United States of America): Lawrence Berkeley National Laboratory.
- (v) NCU/TPC (Taiwan): National Central University and the Taiwan Power Company (Taipower).
- (vi) Quintessa/RWM (United Kingdom): Quintessa Ltd on behalf of Radioactive Waste Management.
- (vii) SNL (United States of America): Sandia National Laboratories.
- (viii) UPC/Andra (Spain/France): Universitat Politècnica de Catalunya, funded by l'Agence nationale pour la gestion des des déchets radioactifs.

2. EXPERIMENTAL DATA

The experiment undertaken by the British Geological Survey (BGS) consisted of a 1D gas injection test performed on a compacted bentonite sample (119.88 mm length x 59.59 mm diameter) supplied by Clay Technology AB (Lund, Sweden) and prepared by BGS, see Daniels and Harrington (2017) for a detailed description of the sample preparation and Harrington and Horseman (2003) for a general description of the employed apparatus.

The test is comprised of two stages; hydration followed by gas testing. After gas breakthrough and a period of gas flow through the sample, the injection pump was stopped whilst the stresses and pore pressures were continuously monitored.

2.1. Sample hydration

After installation, the sample was allowed to equilibrate with the water in the radial filters and backpressure end-closure filter for a period of 7.3 days. Then, the sample was allowed to hydrate for the following 32 days, see monitored stresses and porewater pressures for this period in Figures 2 and 3 respectively.

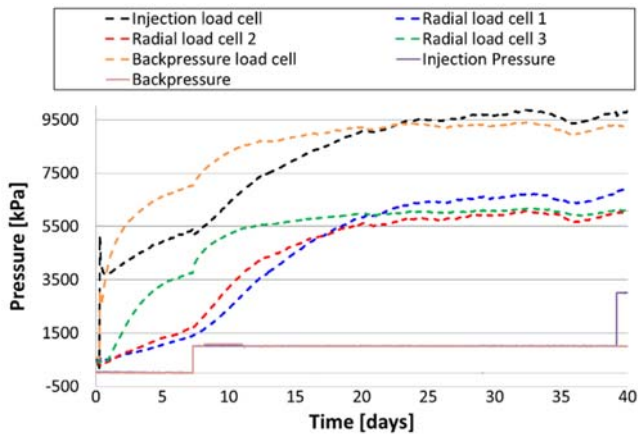


Fig. 2. Swelling pressure measured by the axial and radial load cells, injection pressure and backpressure.

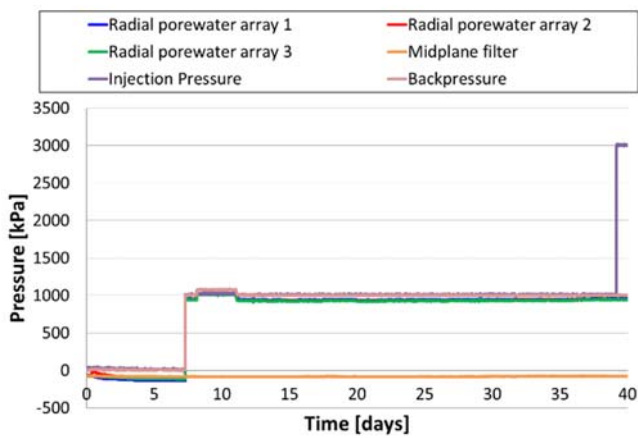


Fig. 3. Axial and radial porewater pressure for the first 40 days. The small deviation in the radial porewater data between days 8-11 is due to using the incorrect pump set-point and was quickly rectified.

2.2. Gas testing

Gas testing began on day 39. Additional helium was added to increase gas pressure to 3 MPa. This was then held constant for a period of 7 days. At day 46, the injection pump was set to a constant flow rate of 500 $\mu\text{L}/\text{h}$ and the injection pressure gradually increased for the next 8 days from 3 MPa to 5 MPa whilst the volume of fluid in the injection pump decreased from 102.7 ml to 6.25 ml. At this point (day 54), the fluid in the injection pump was refilled and the flow rate was reduced to 375 $\mu\text{L}/\text{h}$. At day 61 (before the pressure in the injection filter reached the breakthrough pressure), further helium was added. As such, the injection pump volume increased, see Figures 4 and 5 for the evolution of total stresses and porewater pressures.

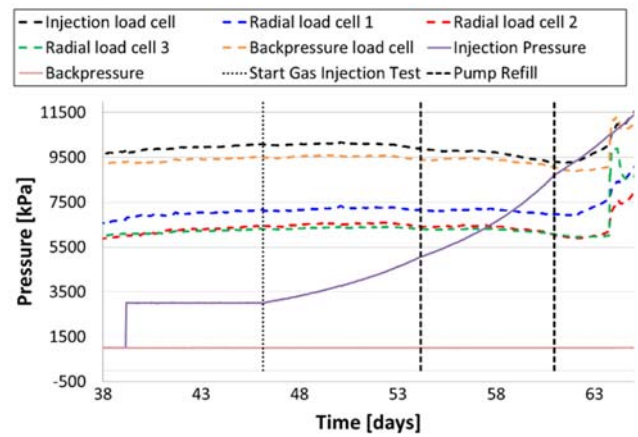


Fig. 4. Total stress up to gas breakthrough at 63.5 days.

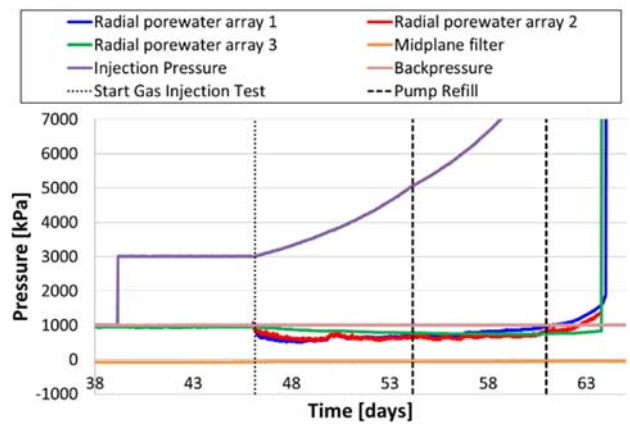


Fig. 5. Porewater pressures up to gas breakthrough at 63.5 days.

Gas breakthrough occurred at 63.5 days. Interestingly, the increase in pressure in the array closest to the injection face lagged behind those of the other two arrays, suggesting non-uniform gas flow. At day 71, the injection pump was stopped. Between day 71 and day 76, the pore pressures decreased substantially, see Figure 6.

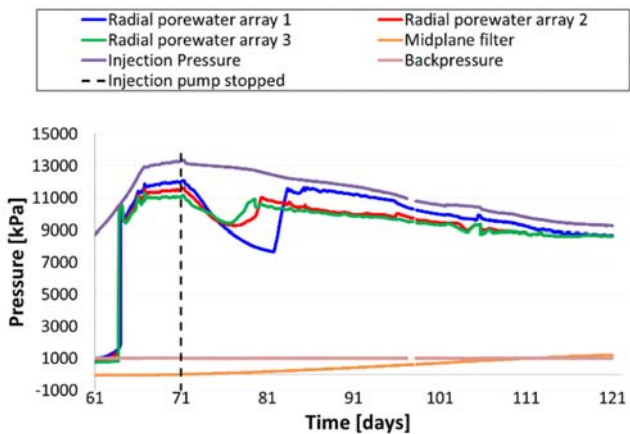


Fig. 6. Injection pressure, backpressure and radial porewater pressure transducer data from day 61 to day 121.

Examination of the axial and radial load cell data during gas entry and breakthrough, Figure 7, indicates that the swelling pressure (stress) within the sample increased at the same time as gas breakthrough occurred in the backpressure filter. Following gas breakthrough, the system approached a quasi-steady state as gas pressure approached an asymptote and flow in and out of the system began to converge (between days 63.5 and 71). The dip in pore pressure seen in Figure 6 between days 71 and 81 also corresponded with a dip in total stress, and an apparent reduction in outflow. This event appears to occur close to the cessation of pumping. However, by day 81, pore pressures rebounded suggesting the cessation of pumping is not the cause for the spontaneous change in pore pressure.

Following gas breakthrough, total stress and pore pressure appeared integrally linked to the gas pressure within the clay. This is in line with previous observations (Harrington and Horseman, 2003; Harrington et al., 2017a). This continued following the cessation of pumping, as gas pressure and total stress and pore pressure began to decay. During this phase of testing, outflow was sporadic suggesting new gas pathways continued to open and close during this phase of testing. Some of these outflow events correlated with observed changes in total stress and pore pressure, while others did not.

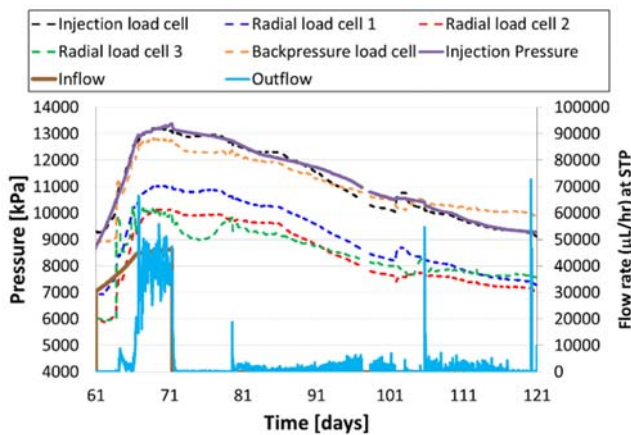


Fig. 7. Total stress and flow data from day 61 to day 121.

3. MODELLING APPROACHES

Different modelling approaches have been adopted by the participating teams:

- (i) Classical two-phase flow models, where basic physical principles such as mass and momentum balance apply for each phase. These standard models have been coupled to different mechanical deformation behaviors in order to better represent the experimentally observed flow. In particular, the

following deformation models have been considered:

- (a) Model UPC/Andra-H, where a rigid porous medium is considered (UPC/Andra).
 - (b) Model LBNL-C, where a linear elastic medium is considered (LBNL).
 - (c) Model CNSC-E, where an elastic medium is assumed (CNSC).
 - (d) Model CNSC-D, where a damage medium is assumed (CNSC).
 - (e) Model KAERI, where a similar damage medium is assumed (KAERI).
 - (f) Model BGR/UFZ, with an elasto-plastic medium (BGR/UFZ).
 - (g) Model NCU/TPC, with a viscoelastic model (NCU/TPC).
- (ii) Enriched two-phase flow models, where preferential pathways are considered:
 - (a) Model Quintessa/RWM: separate gas and water pathways coexist within an elastic deformation matrix (Quintessa/RWM).
 - (b) Models UPC/Andra-HM: two different embedded fracture permeability models have been considered (UPC/Andra). In UPC/Andra-HM1, deformation is modelled assuming elasticity with effective stress and suction terms. In UPC/Andra-HM2, these suction terms are not taken into account.
 - (iii) Discrete approaches:
 - (a) Model LBNL-D: a two-phase flow model within a discrete fracture network (LBNL).
 - (b) Model SNL: a conceptual chaotic model (SNL).

Differences between the proposed strategies also lie in the software used by the teams (Table 1), in the assumed geometry to represent the saturated bentonite (Table 2) and in the fixed/fitted parameters to calibrate the results (Tables 3 and 4 respectively). As seen, some teams (BGR/UFZ, NCU/TPC, UPC/Andra) have used a Young's modulus, initial permeability and porosity values significantly different from those of the material in order to calibrate their models and some models assume a heterogeneous (Het) porosity field.

Table 1. Codes used by the teams.

Model	Software	Reference
BGR/UFZ	OpenGeoSys	Kolditz et al., 2012
CNSC-E	COMSOL Multiphysics®	COMSOL, 2012
CNSC-D		
KAERI	TOUGH-MP FLAC3D	Itasca 1997; Zhang et al., 2008
LBNL-C	TOUGH-FLAC	Rutqvist, 2011
LBNL-D	TOUGH-RBSN	Asahina et al., 2014
NCU/TPC	THMC 7.1	Yeh et al., 2013

Quintessa/RWM	QPAC	Quintessa, 2013
UPC/Andra-H	CODE_BRIGHT	Olivella et al., 1996
UPC/Andra-HM1		
UPC/Andra-HM2		

Table 2. Test geometries used by the teams (Tri = triangle, Quad = quadrilateral, Tetra = tetrahedral, Hex = hexahedral)

Model	Geometry	Mesh	Discretisation
BGR/UFZ	2D axisym.	Tri	2715 elements 1447 nodes
CNSC-E	3D	Tetra	22,000 elements
CNSC-D	3D	Tetra	22,000 elements
KAERI	3D	Hex	7560 elements 8450 nodes
LBNL-C	3D	Hex	23,400 elements 24,939 nodes
LBNL-D	2D	Cells and lattice	1401 cells 3840 lattice elements
NCU/TPC	2D	Quad	1250 elements 1326 nodes
Quintessa/RWM	1D (finite volume)	-	20 cells +1 abstract cell to simulate mass balance in the injector
UPC/Andra-H	3D	Hex	7168 elements 7917 nodes
UPC/Andra-HM1			
UPC/Andra-HM2			

Table 3. Fixed parameters used by the teams.

Model	Basic fixed parameters			
	E [MPa]	ν [-]	ϕ [-]	k [m ²]
BGR/UFZ	307	0.4	0.44	calibrated
CNSC-E	307	0.4	0.44	3.4×10^{-21}
CNSC-D	307	0.4	0.44	3.4×10^{-21}
KAERI	307	0.4	0.44	3.4×10^{-21}
LBNL-C	307	0.4	0.44	3.4×10^{-21}
LBNL-D	307	0.4	Het. 0.44	3.4×10^{-21}
NCU/TPC	307	0.4	0.43	calibrated
Quintessa/RWM	307	0.4	-	3.4×10^{-21}
UPC/Andra-H	-	-	Het. 0.36-0.38	calibrated
UPC/Andra-HM1	225	0.125	Het. 0.36-0.38	calibrated
UPC/Andra-HM2	307	0.44	0.41	calibrated

Table 4. Calibrated parameters used by the teams.

Model	Calibrated parameters
BGR/UFZ	Intrinsic permeability: 1×10^{-21} m ² Critical pressure
CNSC-E	Air-entry value
CNSC-D	Air-entry value Minimum air-entry value Maximum intrinsic permeability Damage smoothing parameter Swelling coefficient
KAERI	Damage parameters: tensile strength, residual tensile strength, tensile strain limit, maximum damage value, maximum permeability
LBNL-C	Hydro-mechanical coupling parameters: swelling coefficient, maximum aperture for stress, reference stress Effective gas-entry pressure value
LBNL-D	Mohr-Coulomb failure parameters Effective gas-entry pressure value Swelling coefficient
NCU/TPC	Intrinsic permeability: 3.4×10^{-22} m ² Air-entry value Viscous parameters
Quintessa/RWM	Capillarity compressibility Capillary spacing Swelling pressure Biot coefficient
UPC/Andra-H	Intrinsic permeability: Het. $k_0 = 5.59 \times 10^{-18}$ m ²
UPC/Andra-HM1	Intrinsic permeability: Het. $k_0 = (2.15 - 7.10) \times 10^{-18}$ m ² Embedded permeability parameters
UPC/Andra-HM2	Intrinsic permeability: Het. $k_0 = (2.15 - 7.10) \times 10^{-19}$ m ² Embedded permeability parameters

3.1. Classical two-phase flow models

Seven different approaches have been proposed. All of them assume the standard van Genuchten (1980) model to describe the water retention curve but they differ in the assumed mechanical deformation behavior.

UPC/Andra developed a two-phase flow calculation on a 3D rigid medium (model UPC/Andra-H). In this model, porosity ϕ [-] is assumed to be space-dependent (randomly generated in the range of 0.36 - 0.38) and intrinsic permeability k [m²] is assumed to be porosity-dependent. The porosity dependence is introduced through the exponential relation

$$k = k_0 e^{b_k(\phi - \phi_0)} \quad (1)$$

where k_0 [m²] is the initial permeability, calibrated to fit experimental data ($k_0 = 5.59 \times 10^{-18}$ m²), b_k [-] is the exponential parameter ($b_k = 60$) and $\phi_0 = 0.37$. The

retention curve is also porosity-dependent and it is computed as

$$S = \left(1 + \left(\frac{p_g - p_w}{p_{VG}} \right)^{\frac{1}{1 - \lambda_{VG}}} \right)^{-\lambda_{VG}} \quad (2)$$

where the shape function $\lambda_{VG} = 0.45$, the gas pressure p_g [Pa] and the water pressure p_w [Pa] are computed according to the van Genuchten model and p_{VG} [Pa] introduces the porosity dependence. Boundary condition of prescribed gas flow in the injection surface is here prescribed.

The three-dimensional linear poro-elastic model LBNL-C is based on an effective stress law that depends on the maximum of the gas- or liquid-phase pressures. A linear moisture swelling effect is also considered: the volumetric swelling of the porous medium's solid skeleton is a function of the saturation of the liquid thus leading to a swelling stress

$$\Delta \sigma'_{sw} = K \Delta S_l \beta_{sw} \quad (3)$$

where σ'_{sw} [Pa] is the swelling stress, K [Pa] is the bulk modulus, S_l [-] is the liquid saturation and β_{sw} [-] is a calibrated moisture swelling coefficient. In this model, a fracture-like behavior of the flow path is assumed. Hence, a pressure P [Pa] dependent gas permeability

$$k = k_{matrix} + \frac{b_h^3}{12a} \quad (4)$$

is considered, where a [m] is the element width and b_h [m] is a non-linear function of the effective minimum compressive stress that reads

$$b_h = \frac{b_{h0}}{1 + 9 \left(\frac{\sigma_n - P}{\sigma_{n,ref}} \right)} \quad (5)$$

with b_{h0} [m] being the (calibrated) maximum aperture for permeability, σ_n [Pa] the total stress normal to the fracture and $\sigma_{n,ref}$ [Pa] the adjusted reference stress normal to the fracture.

The three-dimensional model CNSC-E proposed by CNSC assumes an elastic deformation of the solid material. The pore fluid pressure p [Pa] is here assumed to be dependent on the Bishop's parameter χ [-] as follows

$$p = (1 - \chi)p_g + \chi p_w \quad (6)$$

where χ is a function of the air-entry value (calibrated value to fit experimental data) and suction based on Khalili and Khabbaz, 1998.

An enhanced version of this model (CNSC-D) was also developed by CNSC. In this version, a damaged bulk is considered (Fall et al., 2014) thus accounting for the elastic degradation due to microcracks or damage. Hence,

the stiffness of the material depends on a damage parameter D ($0 \leq D \leq 1$) and reads

$$E = E_0 (1 - D^c) \quad (7)$$

where E_0 [Pa] is the initial stiffness and c [-] is the damage smoothing parameter. Both the air entry value and the intrinsic permeability of this model are also damage dependent. The permeability is computed by means of

$$k = k_{undam.} + k_{dam.}(D) \quad (8)$$

where

$$k_{dam.} = D^c (k_{max} - k_{undam.}) \quad (9)$$

with k_{max} [m²] being the maximum intrinsic permeability (a calibrated parameter). In this model, the swelling induced volume change $d\varepsilon_{vs}$ is related to the change in suction ds by the equation

$$d\varepsilon_{vs} = -B_s ds \quad (10)$$

where B_s [Pa⁻¹] is a calibrated swelling coefficient.

A different damage-based model was proposed by KAERI. Again, bentonite degradation due to microcracks is taken into account by means of a tensile/compressive damage model. The intrinsic permeability of the model is also characterized by Eq. (8) and (9).

In model BGR/UFZ, a critical pressure p_{crit} [Pa] is introduced and calibrated, which is a sum of the minimal principal stress (confining pressure) and the gas entry pressure. The dilatancy pathway is expressed by permeability change (Xu et al., 2013)

$$k = \begin{cases} (1 + 0.0125p_g)k_{int}, & p_g \leq p_{crit} \\ (15.2p_g - 485)k_{int}, & p_g > p_{crit} \end{cases} \quad (11)$$

In model NCU/TPC, a viscoelastic deformation behavior is assumed. In this model, intrinsic permeability is a non-linear function of porosity and reads

$$k = k_0 \left(\frac{1}{1 + (\phi_0 - \phi)} \right)^n \quad (12)$$

where k_0 [m²] and ϕ_0 [-] are the reference intrinsic permeability and the reference porosity respectively and n is the fractional exponent depending on the particle size and packing structure. Note that at this moment in time, see Section 4, this model is not able to correctly reflect the physics of the experiment and further development is needed.

3.2. Enriched two-phase flow models with preferential pathways

Three different enriched two-phase flow continuum models have been considered. In these approaches, the bentonite matrix behaves as a linear elastic medium, where preferential gas pathways are included.

Quintessa/RWM developed a model with separate gas and water pathways. The model considers the saturated bentonite as two components: (i) the clay solid with the non-mobile interlayer water and (ii) the “free” water component. Darcy’s law is assumed to describe the “free” water movement with water permeability k_w [m²]

$$k_w = k_{\text{int}} \quad (13)$$

whereas gas movement is modelled through the Hagen-Poiseuille law. Thus, the opening (and closure) of gas pathways is represented through the capillary radius and its relationship to gas permeability k_g [m²]

$$k_g = \frac{\pi r^4}{8a} \quad (14)$$

where a [m²] is the calibrated capillary spacing. The capillary radius r [m] is considered to be dependent on the capillarity compressibility γ [m²Pa⁻¹] through

$$r = r_0 + \frac{\gamma}{r_0} (\epsilon_c(p_g) - \epsilon_{c0}) \quad (15)$$

where r_0 [m] is the reference capillary radius, ϵ_c [Pa] is the stress for the capillary compressibility, ϵ_{c0} [Pa] is the reference stress for the capillary compressibility and p_g [Pa] is the gas pressure. As seen by means of Eq. (14) and (15), the coupling of the stresses to the permeability is done through the capillarity radius. In order to model the ceasing of gas flow observed in Figure 7, Quintessa/RWM proposed a simple model of the gas injection system based on the ideal gas law.

UPC/Andra developed two different models (UPC/Andra-HM1, UPC/Andra-HM2) to reproduce the development of preferential gas pathways. These two approaches are based on the embedded fracture model proposed by Olivella and Alonso, 2008. The basic idea of this model consists in properly representing single fractures embedded in a continuous matrix. These fractures are characterized by their aperture b [m] and spacing a [m] thus leading to an intrinsic permeability

$$k = k^{\text{mat}} + k^{\text{frac}} = \frac{k_0(1-\phi_0)^2}{\phi_0^3} \frac{\phi^3}{(1-\phi)^2} + \frac{b^3}{12a} \quad (16)$$

where ϕ_0 [-] is the initial porosity, k_0 [m²] is the reference permeability, ϕ [-] is the porosity and a [m] refers to the spacing between fractures. In model UPC/Andra-HM1, the same relative permeability for both matrix and fractures is considered. Hence, gas permeability reads

$$k_g = k_{rg} k = k_{rg} \left(\frac{k_0(1-\phi_0)^2}{\phi_0^3} \frac{\phi^3}{(1-\phi)^2} + \frac{b^3}{12a} \right) \quad (17)$$

where k is defined by Eq. (16). Model UPC/Andra-HM2 assumes different relative permeabilities for the matrix and fractures. Hence, gas permeability reads

$$k = k_{rg}^{\text{mat}} \frac{k_0(1-\phi_0)^2}{\phi_0^3} \frac{\phi^3}{(1-\phi)^2} + k_{rg}^{\text{frac}} \frac{b^3}{12a} \quad (18)$$

3.3. Discrete approaches

LBLN proposed a discrete technique where a two-phase flow model is coupled to a discrete fracture network (DFN). In particular, the rigid-body-spring network (RBSN) approach, which can be categorized as a lattice model and is based on the rigid-body-spring model developed by Kawai (1978), is assumed to characterize the mechanical and fracture-damage behavior. Thus, the fracture process of a local rigid-body-spring element is realized by degrading the springs. Hence, the stiffness matrix reads

$$\mathbf{D} = (1 - D)\mathbf{D} \quad (19)$$

where, similarly as the proposed damage strategies (see Eq. (7)), D is a scalar parameter ($0 \leq D \leq 1$). In LBNL-D model, D is directly switched from 0 to 1 once a fracture event occurs, i.e. once the stress state of an element violates the Mohr-Coulomb criteria. As done by UPC/Andra, see Eq. (16), the permeability is porosity-dependent and reads

$$k = \begin{cases} \frac{k_0(1-\phi_0)^2}{\phi_0^3} \frac{\phi^3}{(1-\phi)^2}, & \text{if unfractured} \\ k_0 + \frac{b^3}{12a}, & \text{if fractured} \end{cases} \quad (20)$$

where again, ϕ_0 [-] is the initial porosity, k_0 [m²] is the reference permeability, ϕ [-] is the porosity, b [m] is the fracture aperture and a [m] is the element width.

Another conceptual model, where special emphasis is placed on the capture of dilatancy was proposed by SNL. This is based on the concept of the delay logistic model (Strogatz, 2001; Bani-Yaghoub, 2017). The model underlying assumption is that given the low permeability of the material, the dominant mechanism for gas migration is first to form a bubble nucleation and then to push the bubble through the clay matrix through matrix dilation and fracturing. Thus, the evolution of mass and pressure within a bubble of a volume V is simply expressed by

$$\frac{dM}{dt} = k_u(P_u - P) - k_d(P - P_d) \quad (21)$$

where M is the gas mass in the bubble (described through the ideal gas law); P is the gas pressure in the bubble; P_u and P_d are the gas pressures in the upstream and the downstream of the bubble movement respectively; k_u and

k_d are the permeability of the matrix in the upstream and the downstream of the bubble movement respectively and assumed to be proportional to P ; and t is the time. Due to its preliminary nature, this novel technique is not taken into account in the comparison analysis of Section 4.

4. RESULTS

Inflow results were analyzed by the teams. However, some modelling teams fitted the inflow into the injection system whereas some other teams calibrated their strategies by means of the inflow into the sample. Thus, the analysis of the inflow modelling results does not provide meaningful information and, finally, it has not been considered.

Figure 8 shows the outflow results, see Table 5 for a summary. Model BGR/UFZ is not able to correctly capture the shape of the post-breakthrough curve (there is some delay with respect to the observed data) but similar peak values are obtained. Similar comments apply to LBNL-C and LBNL-D models; although the peak outflow value is reasonably well captured, the overall shape of the modelled outflow curve is not well described. The two models proposed by CNSC (both CNSC-E and CNSC-D) fail in describing the outflow data and the results are four orders of magnitude smaller than the experimentally observed; whereas the damaged-based KAERI model reasonably describes the shape of the experimentally-observed outflow. The three approaches presented by UPC/Andra fail in fitting this curve. Indeed, although the calculated outflow is slightly better fitted by the hydraulic model (UPC/Andra-H) than by the hydro-mechanical models, the peak value in this case is only about 40% of the observed values. On the contrary, model Quintessa/RWM leads to a good representation of the value at the breakthrough. However, the shape of the simulated curve is not properly captured.

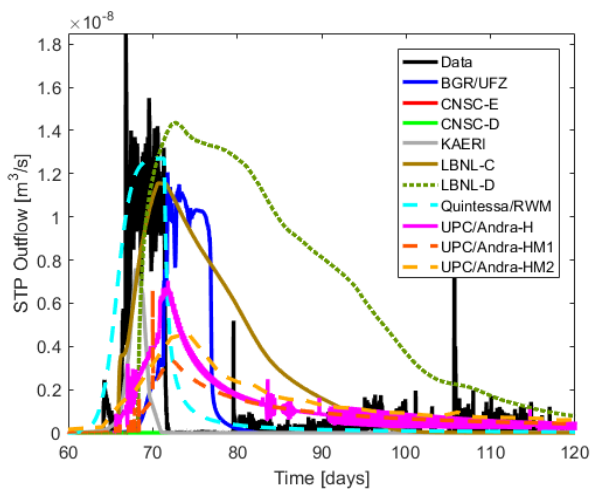


Fig. 8. Comparison of modelled versus observed outflow results.

Table 5. Capabilities of the proposed models regarding flow.

Model	Outflow	
	Peak	Shape
BGR/UFZ	✓	
CNSC-E		
CNSC-D		
KAERI		✓
LBNL-C	✓	
LBNL-D	✓	
NCU/TPC	Not attempted	
Quintessa/RWM	✓	
UPC/Andra-H		
UPC/Andra-HM1		
UPC/Andra-HM2		

Stress results are shown in Figures 9 to 13. As seen, evolution of stress at five different locations has been studied (at the injection load cell, at the backpressure load cell and at three different radial load cells). Although the description of the stress response during the hydration phase (from 0 to 39 days) is a key aspect, little effort was spent by the teams fitting this first stage. As observed, the models Quintessa/RWM and LBNL-C are the only models that properly capture the peak stress value at all the monitored sensors. Model BGR/UFZ is able to correctly capture this value along radial load sensors 1, 2 and 3. However, its prediction of the peak stress value at the backpressure load cell slightly underpredicts the measured value (it should be noted that BGR/UFZ did not postprocess the stress at the injection load cell and thus, BGR/UFZ model cannot be assessed in this point). At the radial load cells 1, 2 and 3, the peak stress value obtained by the rest of the modelling participants either underpredicts the physically-observed quantity (see CNSC-E) or overpredicts it (see damaged-based KAERI model, the hydro-mechanical models by UPC/Andra and the discrete model LBNL-D). CNSC-D is able to capture the peak value at load cell 1 but underpredicted values are obtained at load cells 2 and 3. The predicted value at the injection load cell obtained by UPC/Andra, KAERI and LBNL-D is well defined whereas at the backpressure load cell is underpredicted (UPC/Andra, KAERI) or overpredicted (LBNL-D). The post-peak shape trend is well defined by almost all models and only Quintessa/RWM, CNSC-E and LBNL-C fail in describing the post-peak curve. A visual inspection of the data indicates that many of the teams are able to capture the rapid increase in stress at similar times than the experimentally observed ones. However, simulated curves show precursor events which are not reflected in the data. Models proposed by CNSC and LBNL are the only approaches capable of reasonably capturing the exact timing when breakthrough occurs, see Table 6.

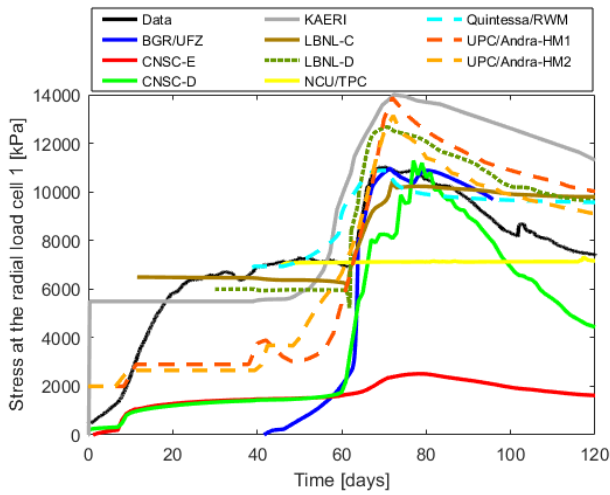


Fig. 9. Comparison of modelled versus observed stress evolution at radial load cell 1.

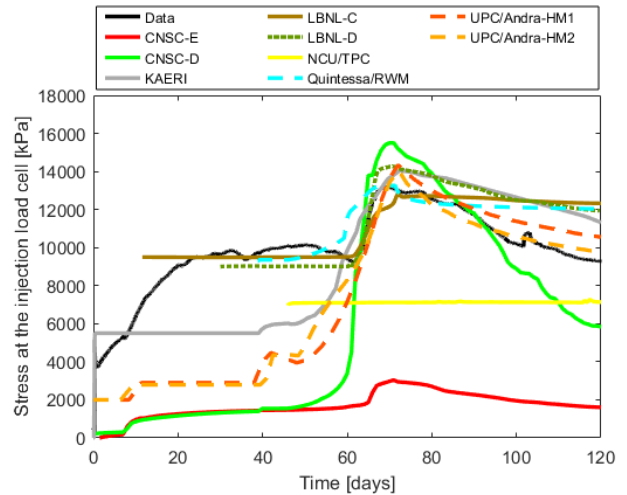


Fig. 12 Comparison of modelled versus observed stress evolution at the injection load cell.

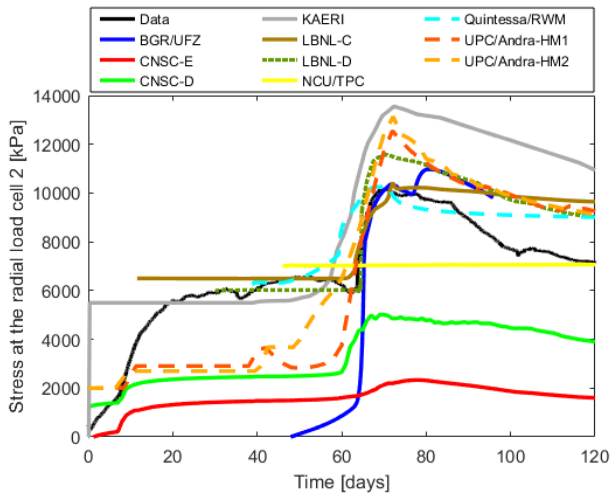


Fig. 10 Comparison of modelled versus observed stress evolution at radial load cell 2.

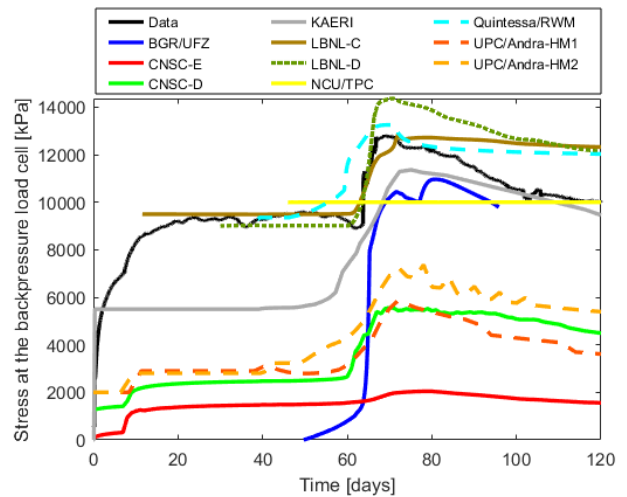


Fig. 13 Comparison of modelled versus observed stress evolution at the backpressure load cell.

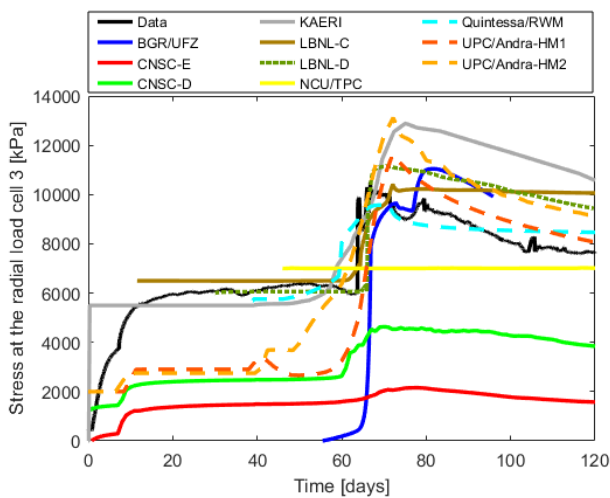


Fig. 11. Comparison of modelled versus observed stress evolution at radial load cell 3.

Table 6. Capabilities of the proposed models regarding stress evolution. Note many of the models without a tick are able to correctly capture the rapid increase in stress but exhibit either a precursor event or start at an incorrect stress value (✓: good, ~: fair, blank: bad, -: results not provided or not applicable).

Model	Stress														
	Peak					Post-peak shape					Timing				
	1	2	3	I	B	1	2	3	I	B	1	2	3	I	B
BGR/UFZ	✓	✓	✓	-	~	✓	✓	✓	-	✓	✓	✓	-	✓	✓
CNSC-E											✓	~	~	✓	✓
CNSC-D	✓			~		✓			✓		✓	~	~	~	~
KAERI				✓	~	✓	✓	✓	✓	✓					
LBNL-C	✓	✓	✓	✓	✓						✓	✓	✓	✓	✓
LBNL-D	~	~	✓	✓	~	✓	✓	✓	✓	✓	✓	✓	✓	✓	✓
NCU/TPC															
Quintessa/RWM	✓	✓	✓	✓	✓									~	
UPC/Andra-H	-														

UPC/Andra-HM1			~	✓	✓	✓	✓	✓	✓	~	✓	~
UPC/Andra-HM2	~		✓	✓	✓	✓	✓	✓	✓			

Pore pressure evolutions at three different locations (arrays 1, 2 and 3) are shown in Figures 14 to 16. It is important to note that before gas breakthrough, pore pressure equals porewater pressure. However, once gas enters the filter, this is actually measuring local gas pressure. As seen, models KAERI, LBNL-D and UPC/Andra-HM2 are able to properly capture the peak value at all the arrays. The continuous model proposed by LBNL provides good predicted peak values in sensors 1 and 2 but the breakthrough pore pressure at sensor 3 is slightly overpredicted. Reasonably good peak values are also obtained with BGR/UFZ and UPC/Andra-HM1 models. However, at these arrays, highly overpredicted (with model UPC/Andra-H) and underpredicted (CNSC-E, CNSC-D, Quintessa/RWM) values are also obtained. As happened with the stress response, (i) the post-peak shape trend is well defined by almost all models and only Quintessa/RWM and CNSC-E fail in describing the post-peak curve (now model LBNL-C provides good post-peak shape fitting) and (ii) the two models proposed by CNSC and LBNL are the only approaches capable of properly capturing the timing when breakthrough occurs, see Table 7. As happened also with the stress response, the rapid increase in pore pressure is modelled by many of the teams. However, this is obtained at early times by some of them.

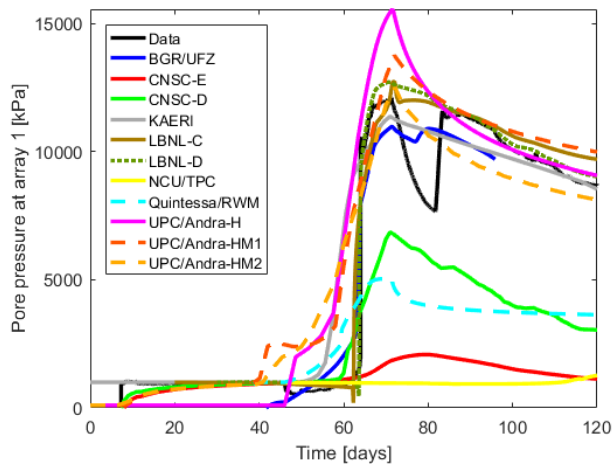


Fig. 14. Comparison of modelled versus observed pore pressures at array 1.

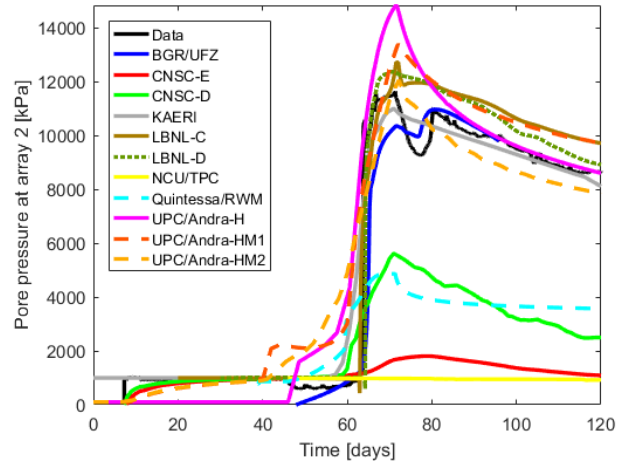


Fig. 15. Comparison of modelled versus observed pore pressures at array 2.

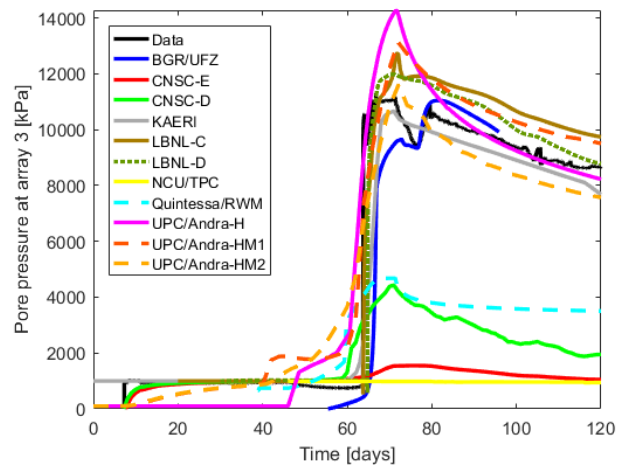


Fig. 16. Comparison of modelled versus observed pore pressures at array 3.

Table 7. Capabilities of the proposed models regarding porewater evolution (✓: good, ~: fair, blank: bad).

Model	Porewater pressure								
	Peak			Post-peak shape			Timing		
	1	2	3	1	2	3	1	2	3
BGR/UFZ	✓	~	~	✓	✓	✓			✓
CNSC-E							✓	✓	✓
CNSC-D				✓	✓	✓	~	~	~
KAERI	✓	✓	✓	✓	✓	✓			✓
LBNL-C	✓	✓	~	✓	✓	✓	✓	✓	✓
LBNL-D	✓	✓	✓	✓	✓	✓	✓	✓	✓
NCU/TPC									
Quintessa/RWM									~
UPC/Andra-H				✓	✓	✓			
UPC/Andra-HM1	~	~	~	✓	✓	✓	~	~	~
UPC/Andra-HM2	✓	✓	✓	✓	✓	✓			

5. CONCLUSIONS AND FUTURE WORK

The different modelling teams have shown that a wide range of models may be applied to numerically describe gas migration in plastic clays. At this stage of the modelling exercise, models have been validated against a single experiment and thus, future work is still needed to further develop them. So far, existing fits show that after a calibration process (often a very large set of input parameters need to be adjusted), plausible descriptions of the laboratory experiment can be achieved. In a number of cases, these realizations required adjustment of porosity and intrinsic permeability values beyond specified parameters for the material, suggesting the physical description of the system remains incomplete.

Two-phase flow models (with different deformation behaviors and/or preferential pathways) have been implemented to model gas flow. These approaches are able to match some key aspects such as stress evolution or pore pressure. However, they are not capable of describing the full complexity of gas migration processes in such low-permeability materials. Thus, although they are highly extended and employed, the modelling to date suggests that they are not capable of reproducing the full range of behavior exhibited in the experiment, so their practicality will depend upon the intended usage. Discrete approaches to describe dilatancy-controlled gas flow may lead to physically plausible representations. However, an extra effort is needed to calibrate the very large set (even larger) of input parameters. New conceptual models may be hence developed to explain this complexity. However, their development is still in a very preliminary phase and at the current stage of the work, they are not able to reproduce physically-observed features. Thus, from a pragmatic perspective, enhanced two-phase flow models (either by different deformation behaviors, explicitly incorporating different pathways and/or evolving fractures) remain the only viable tool to represent these systems at this time. However, the complexity of the physical processes combined with detailed calibration processes, currently limit their use in the quantitative prediction of gas flow. Hence, further work is required:

- Models will be validated against more complex data sets. This will take the form of a spherical flow test in which the spatial distribution of flow was measured. Knowledge from this three-dimensional test will be used to further develop the existing models.
- Some models will be simplified to reduce the number of fitting parameters. In addition, the data will be compartmentalized into different test stages to better facilitate validation of the models.

ACKNOWLEDGEMENTS

[DECOVALEX](#) is an international research project comprising participants from industry, government and academia, focusing on development of understanding, models and codes in complex coupled problems in sub-surface geological and engineering applications; DECOVALEX-2019 is the current phase of the project. The authors appreciate and thank the DECOVALEX-2019 Funding Organisations Andra, BGR/UFZ, CNSC, US DOE, ENSI, JAEA, IRSN, KAERI, NWMO, RWM, SÚRAO, SSM and Taipower for their financial and technical support of the work described in this paper. The statements made in the paper are, however, solely those of the authors and do not necessarily reflect those of the Funding Organisations.

The first two authors thank Dr. Robert Cuss for his comments to improve the manuscript. The third author would like to thank Torben Brüning for his hard work on the parameter variation and data preparation. This paper is published with the permission of the Executive Director, British Geological Survey (NERC).

REFERENCES

1. Angeli, M., M. Soldal, E. Skurtveit and E. Aker. 2009. Experimental percolation of supercritical CO₂ through a caprock. *Energy Procedia*. 1, 3351-3358.
2. Asahina, D., J.E. Houseworth, J.T. Birkholzer, J. Rutqvist, J.E. Bolander. 2014. Hydro-mechanical model for wetting/drying and fracture development in geomaterials. *Computers & Geosciences*, 65, 13-23.
3. Bani-Yaghoub, M. 2017. Analysis and applications of delay differential equations in biology and medicine, arXiv:1701.04173v1.
4. COMSOL. 2012. COMSOL Multiphysics version 3.5 User's Guide.
5. Daniels, K.A. and J.F. Harrington. 2017. The Response of Compact Bentonite during a 1D Gas Flow Test. British Geological Survey Open Report, OR/17/067. 19pp.
6. Fall, M., O. Nasir, T.S. Nguyen. 2014. A coupled hydro-mechanical model for simulation of gas migration in host sedimentary rocks for nuclear waste repositories. *Engineering Geology*. 176, 24-44.
7. Harrington, J.F., S.T. Horseman. 1999. Gas transport properties of clays and mudrocks. In *Muds and Mudstones: Physical and Fluid Flow Properties*, ed. A.C. Aplin, A.J. Fleet and J.H.S. Macquaker. Geological Society of London Special Publication, 158. Geological Society of London, London, 107-124.
8. Harrington, J.F. and S.T. Horseman. 2003. Gas migration in KBS-3 buffer bentonite: Sensitivity of test parameters to experimental boundary conditions. *Report TR-03-02*. Svensk Kärnbränslehantering AB (SKB), Stockholm, Sweden.

9. Harrington, J.F., C.C. Graham, R.J. Cuss and S. Norris. 2017a. Gas network development in a precompacted bentonite experiment: Evidence of generation and evolution. *Applied Clay Science*, 147, 80-89.
10. Harrington, J.F., R.J. Cuss and J. Talandier. 2017b. Gas transport properties through intact and fractured Callovo-Oxfordian mudstones. In: Rutter, E. H., Mecklenburgh, J. & Taylor, K. G. (eds) *Geomechanical and Petrophysical Properties of Mudrocks*. Geological Society, London, Special Publications, 454., <https://doi.org/10.1144/SP454.7>
11. Horseman, S.T., J.F. Harrington and P. Sellin. 1996. Gas migration in Mx80 buffer bentonite. *Materials Research Society*, 465, 1003-1010.
12. Horseman, S.T., J.F. Harrington and P. Sellin. 2004. Water and gas flow in Mx80 bentonite buffer clay. *Materials Research Society*, 807, 715-720.
13. Itasca, FLAC3D Version 2.0, 1997. Fast Lagrangian Analysis of Continua in 3 Dimensions. *ITASCA Consulting Group Inc.*
14. Kawai, T. 1978. New discrete models and their application to seismic response analysis of structures. *Nuclear Engng. Design*, 48, 207-229.
15. Khalili, N., M.H. Khabbaz. 1998. A unique relationship for χ for the determination of the shear strength of unsaturated soils. *Géotechnique* 48, 1-7.
16. Kolditz, O., S. Bauer, L. Bilke, N. Böttcher, J.O. Delfs, T. Fischer, U.J. Görke, T. Kalbacher, G. Kosakowski, C.I. McDermott, C.H. Park, F. Radu, K. Rink, H. Shao, H.B. Shao, F. Sun, Y.Y. Sun, A.K. Singh, J. Taron, M. Walther, W. Wang, N. Watanabe, N. Wu, M. Xie, W. Xu, B. Zehner. 2012. OpenGeoSys: An open-source initiative for numerical simulation of thermo-hydro-mechanical/chemical (THM/C) processes in porous media. *Environ. Earth Sci.* 67, 589-599.
17. Marschall P., S. Horseman, T. Gimmi. 2005. Characterisation of gas transport properties of the Opalinus Clay, a potential host rock formation for radioactive waste disposal. *Oil & Gas Science and Technology – Revue de l'Institut Francais Petrole*, 60:121-139.
18. Olivella, S., A. Gens, J. Carrera, E.E. Alonso. 1996. Numerical formulation for a simulator (CODE_BRIGHT) for the coupled analysis of saline media, *Engineering Computations*, 13: 7, 87-112.
19. Olivella, S., E.E. Alonso. 2008. Gas flow through clay barriers. *Géotechnique* 58:3, 157-176.
20. Ortiz, L., G. Volckaert and D. Mallants. 2002. Gas generation and migration in Boom Clay, a potential host rock formation for nuclear waste storage. *Engineering Geology*, 64, 287-296.
21. Quintessa. 2013. QPAC: Quintessa's General-Purpose Modelling Software QRS-QPAC-11. <http://www.quintessa.org/qpac-overview-report.pdf>
22. Rutqvist, J. 2011. Status of the TOUGH-FLAC simulator and recent applications related to coupled fluid flow and crustal deformations, *Computers & Geosciences*, 37, 739-750.
23. Strogatz, S.H. 2001. *Nonlinear Dynamics and Chaos: With Applications to Physics, Biology, Chemistry, and Engineering*, Westview.
24. van Genuchten, M.T. 1980. A closed-form equation for predicting the hydraulic conductivity of unsaturated soils. *Soil science society of America journal* 44: 892-898.
25. Weetjens, E. and X. Sillen. 2006. Gas Generation and Migration in the Near Field of a Supercontainer-Based Disposal System for Vitrified High-Level Radioactive Waste. In *Proceedings of the 11th International High-Level Radioactive Waste Management Conf. (IHLRWM), Las Vegas, Nevada, USA, April 30 – May 4.*
26. Wikramaratna, R.S., M. Goodfield, W.R. Rodwell, P.J. Nash and P.J. Agg. 1993. A Preliminary Assessment of Gas Migration from the Copper/Steel Canister. *SKB Technical report TR93-31.*
27. Xu, W.J., H. Shao, J. Hesser, W. Wang, K. Schuster and O. Kolditz, 2013. Coupled multiphase flow and elastoplastic modelling of in-situ gas injection experiments in saturated claystone (Mont Terri Rock Laboratory). *Engineering Geology*, 157, 55-68.
28. Yeh, G.T., C.H. Tsai and I.S. Liu. 2013. GMech: A Geo-Mechanics Model for Finite Visco-Elastic Materials: Theoretical Basis and Numerical Approximation. Graduate Institute of Applied Geology, National Central University, Zhongli City, Taoyuan County, Taiwan.
29. Zhang, K. Y.S. Wu and K. Pruess. 2008. User's guide for TOUGH2-MP- A massively parallel version of the TOUGH2 code. *Earth Sciences Division, Lawrence Berkeley National Laboratory.*